Supplementary Materials for

Shrinking light to allow forbidden transitions on the atomic scale

Nicholas Rivera,* Ido Kaminer, Bo Zhen, John D. Joannopoulos, Marin Soljačić

*Corresponding author. Email: nrivera@mit.edu

This PDF file includes:

Supplementary Text

Figs. S1 to S5

References and Notes

Contents

1   Introduction

In this appendix, we outline the use of quantum electrodynamics (QED) for computing decay rates of atomic excited states due to the vacuum macroscopic electromagnetic fields associated with 2D conductors. We consider atom-field interactions governed by the non-relativistic Pauli-Schrodinger Hamiltonian H:

$$H = H_a + H_{em} + H_{int}$$

$$H_a = \left(\sum_i \frac{\mathbf{p}_i^2}{2m_e} - \frac{e^2}{4\pi\epsilon_0 r_i} \right) + H_{e-e} + H_{SO}$$

$$H_{em} = \sum_{j=x,y,z} \int d\mathbf{r} \int d\omega \, \hbar\omega \left(f_j^\dagger(\mathbf{r},\omega) f_j(\mathbf{r},\omega) + \frac{1}{2} \right)$$

$$H_{int} = \sum_i \frac{e}{2m} (\mathbf{p}_i \cdot \mathbf{A}(\mathbf{r}_i) + \mathbf{A}(\mathbf{r}_i) \cdot \mathbf{p}_i) + \frac{e^2}{2m} \mathbf{A}^2(\mathbf{r}_i) + \frac{e\hbar}{2m} \boldsymbol{\sigma}_i \cdot \mathbf{B}(\mathbf{r}_i), \qquad \text{(S1)}$$

where H_{e-e} is the electron-electron interaction, H_{SO} is the spin-orbit coupling, H_a is the atomic Hamiltonian, H_{int} is the atom-field interaction, $\mathbf{A}$ is the vector potential operator, and $\mathbf{B}$ is the magnetic field operator. The operators (and notation) appearing in the field energy, given by H_{em}, will be explained in Sec. II. The minimal-coupling interaction Hamiltonian presented above is related to the more well-known dipole interaction Hamiltonian: $-\mathbf{d} \cdot \mathbf{E} +$ self-energy, by a unitary transformation in the long-wavelength (dipole) approximation (*48*).

Because the atoms that we consider are interacting with dissipative media, the canonical quantization based on the mode expansion of the electromagnetic field is not valid. Instead we

must use the formalism of macroscopic QED. For more information about macroscopic QED, see Refs. (*52, 53*). We also discuss conditions for which a canonical quantization scheme based on the expansion of lossless modes is a suitable approximation for the decay rate of an excited atom. We choose a fully quantum mechanical approach rather than the well known phenomenological approach based on the LDOS not only because it takes into account the orbital and spin degrees of freedom of the emitter, but also because it provides an elegant way to compute rates of transitions with varying multipolarity. Moreover, for higher-order processes in QED, a quantum approach becomes clearly necessary.

2 Macroscopic QED of 2D Conductors

Choosing a gauge in which the scalar potential is identically zero, the vector potential operator is given by:

$$A_i(\mathbf{r}) = \sqrt{\frac{\hbar}{\pi\epsilon_0}} \int d\omega' \frac{\omega'}{c^2} \int d\mathbf{r}' \sqrt{\text{Im } \epsilon(\mathbf{r}', \omega')} \mathbf{G}_{ij}(\mathbf{r}, \mathbf{r}'; \omega') \hat{f}_j(\mathbf{r}', \omega') + \text{H.c.,} \qquad \text{(S2)}$$

where $\mathbf{G}_{ij}$ is the dyadic Green function of the Maxwell equations, satisfying $\nabla \times \nabla \times \mathbf{G}_i - \epsilon(\mathbf{r}, \omega)\frac{\omega^2}{c^2}\mathbf{G}_i = \delta(\mathbf{r} - \mathbf{r}')\hat{e}_i$. Physically it represents the field at point $\mathbf{r}$ produced by a time-harmonic dipole at $\mathbf{r}'$ oriented along direction i. $\hat{\mathbf{f}}_j^{(\dagger)}(\mathbf{r}, \omega)$ annihilates (creates) an excitation of frequency ω, at position $\mathbf{r}$, and oriented along direction j. It satisfies bosonic commutation relations, namely: $\left[\hat{f}_i(\mathbf{r}, \omega), \hat{f}_j^\dagger(\mathbf{r}', \omega')\right] = \delta_{ij}\delta(\omega - \omega')\delta(\mathbf{r} - \mathbf{r}')$. When applying the Fermi Golden Rule, the initial state is $|e, 0\rangle$, while the final states are of the form $|g, \mathbf{x}\omega k\rangle \equiv \hat{f}_k^\dagger(\mathbf{x}, \omega)|g, 0\rangle$

(*52*). Using these final states in addition to the commutation relations, we get that [1]

$$\Gamma = \frac{2\pi}{\hbar^2} \frac{e^2\hbar}{\pi\epsilon_0 m_e^2 c^2} \int d\mathbf{x} \sum_k \frac{\omega_0^2}{c^2} \text{Im } \epsilon(\mathbf{x}) \left| \langle e | G_{ik} p_i(\mathbf{r}, \mathbf{x}, \omega_0) | g \rangle \right|^2.$$

Expanding the matrix element yields:

$$\Gamma = \frac{2\pi}{\hbar^2} \frac{e^2\hbar}{\pi\epsilon_0 m_e^2 c^2} \int \int d\mathbf{r} d\mathbf{r}' \, \psi_e^*(\mathbf{r})\psi_e(\mathbf{r}') \left(\text{Im } G_{ij}(\mathbf{r}, \mathbf{r}', \omega_0) \right) (p_i\psi_g(\mathbf{r}))(p_j^*\psi_g^*(\mathbf{r}')),$$

where we have used the identity: $\frac{\omega_0^2}{c^2} \int d\mathbf{x} \, \text{Im } \epsilon(\mathbf{x}, \omega_0)(G(\mathbf{r}, \mathbf{x}, \omega_0)G^\dagger(\mathbf{r}', \mathbf{x}, \omega_0))_{ij} = \text{Im } G_{ij}(\mathbf{r}, \mathbf{r}', \omega_0)$

(*52*). To proceed, we will substitute in the reflected part of the Green function for the system in Figure 1. We assume a real and non-dispersive permittivity ϵ_r throughout (for simplicity), although this formalism can easily accommodate substrate dispersion and losses. Experimentally, complications arising from the substrate can be alleviated by interfacing graphene with hBN or having free-standing graphene. An exact expression for the Green function can be written in terms of the reflection and transmission coefficients of the interface between the conductor and air (*53,54*). In the air region ($z > 0$):

$$G_{ij}(\mathbf{r}, \mathbf{r}', \omega_0) = \frac{i}{2} \frac{1}{(2\pi)^2} \int d\mathbf{q} \, (C_{ij}^s + C_{ij}^p)e^{i\mathbf{q}\cdot\boldsymbol{\rho}+ik_\perp z}e^{-i\mathbf{q}\cdot\boldsymbol{\rho}'+ik_\perp z'}, \tag{S3}$$

where C^s and C^p are tensors describing the s- and p-polarized parts of the reflected fields. Note that we only need the $z > 0$ solution because the atomic wavefunctions, for the atom-surface separations chosen, decay very rapidly (on the scale of angstroms, as opposed to the decay on the scale of nanometers of the plasmon field), and thus are negligible at the surface.

Choosing the atomic wavefunctions to be real (which can always be done in the cases we consider) and defining $M_i = \int d\mathbf{r} \, \psi_g e^{i\mathbf{q}\cdot\boldsymbol{\rho}+ik_\perp z}p_i\psi_e$, and $M_i^- = \int d\mathbf{r} \, \psi_g e^{-i\mathbf{q}\cdot\boldsymbol{\rho}+ik_\perp z}p_i^*\psi_e$, we

---

[1]Note that we have neglected the $\nabla \cdot \mathbf{A}$ term. This term is (in our gauge), only nonzero at surface of the 2D conductor (and is proportional to a delta function). For the atom-surface separations we chose, the contribution from this term is negligible because the atomic wavefunctions decay very rapidly away from the atomic center and thus provide an extremely weak contribution at the surface. By the way, this is the same reason that "symmetry" effects are irrelevant here, i.e., that the change from 3D translational symmetry (in free-space) to 2D translational symmetry doesn't completely change selection rules. The fact that the atomic wavefunctions only effectively see a plane wave (with complex wave-vector) implies that the atom is interacting with modes formally identical to those in free-space (albeit with a much larger wavevector).

4

arrive at a generalized Fermi Golden Rule:

$$\Gamma = \frac{e^2}{\hbar\epsilon_0 m_e^2 c^2}\text{Re}\left[\frac{1}{(2\pi)^2}\int d\mathbf{q}\; M_i(C_{ij}^s + C_{ij}^p)M_j^-\right]. \tag{S4}$$

The part of the decay rate coming from surface plasmons comes from the p-polarized (transverse magnetic) waves, and accordingly, we will only work with that part of the reflected Green function.

Performing a rotation: $\{x, y, z\} \to \{q, q_\perp, z\}$, C_p can be expressed as

$$-c^2\frac{r_p q}{\omega_0^2}\begin{pmatrix}\frac{k_\perp}{q} & 0 & 1\\ 0 & 0 & 0\\ -1 & 0 & -\frac{q}{k_\perp}\end{pmatrix} = -c^2\frac{r_p q}{\omega_0^2}\begin{pmatrix}\frac{k_\perp}{q}\\ 0\\ -1\end{pmatrix}\otimes\begin{pmatrix}1 & 0 & \frac{q}{k_\perp}\end{pmatrix} \equiv -2ic^2\frac{r_p q}{\omega_0^2}\hat{\epsilon}_i(\mathbf{q})\hat{\epsilon}_j(\mathbf{q})^*,$$

where the polarization vectors are defined by: $\hat{\epsilon}(\mathbf{q}) \equiv \frac{\hat{\mathbf{q}}+i\hat{\mathbf{z}}}{\sqrt{2}}$. We make our first approximation here: the electrostatic limit. Namely, that the main contribution to this integral comes from $q \gg \frac{\omega}{c}$ (i.e., the confinement factor of the emitted plasmons is much larger than 1). This is an excellent approximation in all of our calculations. To lowest order in this approximation: $k_\perp = iq$, and $M_i^- = M_i^*$. Thus,

$$\Gamma = \frac{2e^2}{\hbar\epsilon_0 m_e^2\omega_0^2}\text{Im}\left[\frac{1}{(2\pi)^2}\int d\mathbf{q}\; q|\langle g|(\hat{\epsilon}(\mathbf{q})\cdot\mathbf{p})e^{i\mathbf{q}\cdot\boldsymbol{\rho}-qz}|e\rangle|^2 r_p\right].$$

The Fresnel reflection coefficient in the electrostatic limit is given by $\frac{(\epsilon_r-1)i-\frac{\sigma q}{\omega_0\epsilon_0}}{(\epsilon_r+1)i-\frac{\sigma q}{\omega_0\epsilon_0}}$ (27). Performing a non-dimensionalization on q with respect to q_0: $q = q_0 u$, where $q_0 \equiv \frac{(\epsilon_r+1)\epsilon_0\omega_0}{\sigma_I(\omega_0)}$, we arrive at a relatively simple final result:

$$\Gamma = \frac{4\alpha\omega_0}{m_e^2 c^2(\epsilon_r+1)}\eta_0^3\int d\theta du\; u^2 e^{-2\eta_0 k z_0 u}|\langle g|(\hat{\epsilon}(\mathbf{q})\cdot\mathbf{p})e^{i\mathbf{q}\cdot\boldsymbol{\rho}-q(z-z_0)}|e\rangle|^2\left(\frac{1}{\pi}\frac{\frac{\sigma_R u}{\sigma_I}}{(\frac{\sigma_R u}{\sigma_I})^2 + (1-u)^2}\right), \tag{S5}$$

where η_0 is the resonant confinement factor of the plasmon $\frac{\lambda_0}{\lambda_{pl}}$, $\sigma_R(\sigma_I)$ are the real (imaginary) parts of the (local) conductivity at the resonant frequency, and $\alpha = \frac{e^2}{4\pi\epsilon_0\hbar c}$ is the fine-structure constant. In the lossless limit $(\frac{\sigma_R}{\sigma_I} \to 0)$, the lineshape in parentheses becomes $\delta(u-1)$. The

decay rate in the lossless limit can be understood as the decay rate into surface plasmons (SPs). Note that when a plasmon mode exists ($\sigma_I > 0$), the integrand in Equation (S5) approximately takes the form of a Lorentzian centered around the wavevector of the mode at frequency ω_0. The effective quality factor is σ_I/σ_R, which is a function of ω in the regime where the response is well-described as spatially local. Strictly speaking, the effective quality factor depends on both frequency and wavevector.

Note that in the lossless limit, we arrive at the same expression for the decay rate as would be obtained had we written $\mathbf{A}$ based on a canonical quantization scheme. Namely: $\mathbf{A} = \sum_n \sqrt{\frac{\hbar}{2\epsilon_0 \omega_n}} \left(\mathbf{F}_n a_n + \mathbf{F}_n^* a_n^\dagger \right)$, where the $\mathbf{F}_n$ are the orthonormal modes of the Maxwell equations. In this case, the modes $\mathbf{F}(\mathbf{q})$ are given by: $\sqrt{\frac{2\kappa}{1+\epsilon_r}} e^{i\mathbf{q}\cdot\rho - \kappa z} \left(\frac{\kappa\hat{\mathbf{q}} + iq\hat{\mathbf{z}}}{\sqrt{\kappa^2 + q^2}} \right)$. In the electrostatic limit, $\kappa \approx q$, reproducing the results that we arrive at using the Green function formalism. This provides a cross-check on the results we shall derive below, which take the effects of losses into consideration.

3 First Order Processes

In this section, we consider processes that can be described at first-order in perturbation theory: direct emission into a single excitation of the medium-assisted macroscopic electromagnetic field. In particular, we examine electric multipolar and magnetic multipolar (spin-flip) transitions. We provide a detailed discussion of how losses modify the decay rates computed from canonical quantization based on modal expansion and show the regimes in which non-radiative or radiative decay dominates. By radiative decay, we do not mean decay into far-field photons, but rather into propagating plasmons. This is in contrast to the non-radiative decay into the other lossy channels of the 2D conductor, which, for example, is the mechanism responsible for the strong decay rate enhancement of emitters adsorbed onto a conducting surface.
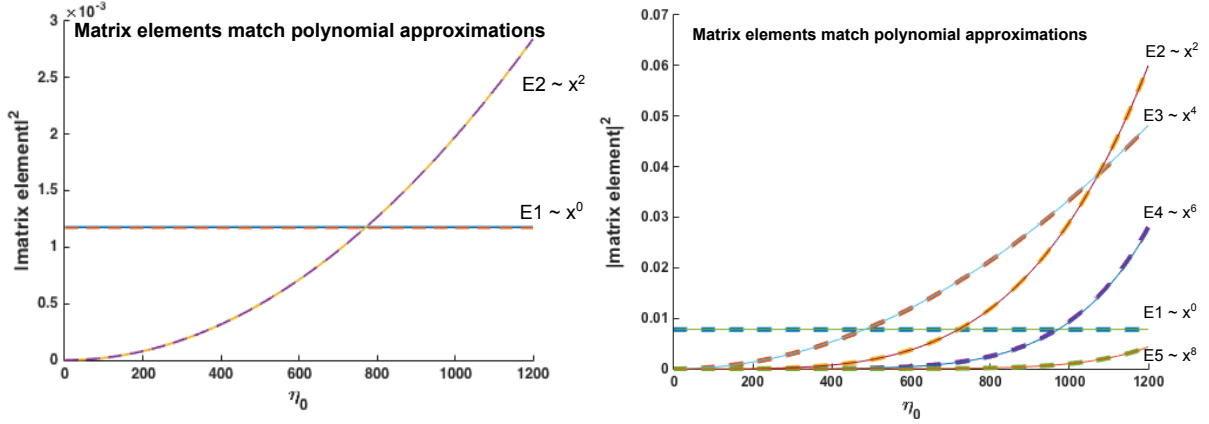
Figure S1: Comparison of matrix elements computed exactly (solid) with polynomial approximations (dashed) for different transitions in the hydrogen $3 \leftrightarrow 4$ transition series (A) and the $5 \leftrightarrow 6$ transition series (B) as a function of η_0 for $\lambda_0 = 1.88$ μm and 7.45 μm (respectively). These curves overlap completely in this range.

3.1 Electric Multipole Transitions

The calculations below are presented for the case for which the initial and final wavefunctions have their z-projected angular momentum to be zero (i.e; $m_i = m_f = 0$). In this case, the angular integral is simply 2π, and we can pick $\mathbf{q}$ to be in a particular direction, called x. Frequently, it is the case that in the matrix element in Equation (S5) there is one main contributing term from the series expansion of the exponential. That is to say:

$$\left| \langle e | e^{\eta_0 k(-ix-(z-z_0))} \hat{e}_\theta^* \cdot \nabla | g \rangle \right|^2 = C_\ell \eta_0^{2(n-1)} u^{2(n-1)} \tag{S6}$$

where $n = 1$ for dipole (E1) transitions, $n = 2$ for quadrupole (E2) transitions, and so on. In Figure S1, we demonstrate the validity of (S6), where we plot exact matrix elements involving the full exponential (solid lines) and their respective polynomial approximations (dashed lines) for E1-E2 transitions in the hydrogen ($4s \leftrightarrow 3\{p, d\}$) transition series (A) and E1-E5 transitions in the hydrogen $6\{p, d, f, g, h\} \rightarrow 5s$ transition series (B) as a function of confinement η_0. These transition series are different than that considered in the main text ($4s \leftrightarrow 6\{p, d, f, g, h\}$).

We choose a different transition series here in order to give the reader a more complete picture of how confinement, separation, vacuum wavelength, and losses affect the decay rates of excited emitters.

When the approximation in Equation (S6) is satisfied, the radiative rate of emission (into surface plasmons) scales with η_0 as:

$$\Gamma_r^{En} = \eta_0^{3+2(n-1)} \times \frac{4\pi\alpha\omega_0}{(m_e c)^2(\epsilon_r + 1)} e^{-2\eta_0 k z_0} C_n.\tag{S7}$$

and the ratio of total decay rate to decay rate into SPs is:

$$\frac{\Gamma_{TOT}^{En}}{\Gamma_R^{En}} = \int du\ u^{2+2(n-1)} e^{-2\eta_0 k z_0(u-1)} \left(\frac{1}{\pi} \frac{\frac{\sigma_R u}{\sigma_I}}{(\frac{\sigma_R u}{\sigma_I})^2 + (1-u)^2} \right)\tag{S8}$$

To gain insight into the typical values of decay rates given by Equations (S7) and (S8), it is useful to write the momentum matrix element in units of $\frac{\hbar}{a_0}$, where a_0 is some characteristic size of the emitter. When considering atomic systems, it is reasonable to take a_0 to be the Bohr radius, in which case C_l is dimensionless and the resulting factor $\left(\frac{\hbar}{m_e c a_0}\right)^2$ is identified as α^2. Our formulas summarized at the end of the SM reflect this choice of units.

3.1.1 Effect of Losses

In Figure S2, we plot this ratio for five Hydrogen atom transitions: $5s \leftrightarrow 6\{p, d, f, g, h\}$. For each transition, we plot the ratio as a function of on-resonance confinement factor η_0 at atom-surface separations of 5 nm, 10 nm, and 15 nm. Note that only the dipole case is not plotted on a logarithmic scale - indicating that losses only weakly modify decay rates of dipole emitters, even for η_0 as low as 20. At very low plasmon confinement, the emission into lossy channels dominates the emission into plasmons. As can be seen in Figure S2, emission into lossy channels far exceeds emission into SPs for higher-order angular momentum transitions. For a Hydrogen atom 5 nm above the a surface undergoing an E5 transition ($6h \rightarrow 5s$), the lossy channel emission can exceed the SP emission by nearly 12 orders of magnitude at $\eta_0 = 20$,

leading to a total Purcell factor of roughly 10^{26}. This leads to a total decay lifetime on the order of 10 ns, which is typical of many dipole emitters in free space.

At higher values of confinement ($\eta_0 > 150$) and atom-surface separation ($z_0 > 10$ nm), the SP and lossy channel decay rates are within the same order of magnitude. While the non-radiative enhancement decreases precipitously at these confinements and separations, the more rapidly increasing enhancement of emission into propagating SPs ensures that the total decay rate is increasing as a function of η_0. To give the reader further intuition for the phenomena discussed in this section, we present in Figure S3 the integrand of Equation (S8) for different values of confinement and atom-surface separation. We place a high-wavevector cutoff in the integrand at a wavelength of 5 nm due to the fact that the use of macroscopic electrodynamics becomes begins to come into question at these distances. The choice of 5 nm is somewhat arbitrary, but we choose it because averaging microscopic fields over a 5 nm $\times$ 5 nm area corresponds to averaging over several hundred unit cells. 5 nm is a somewhat conservative cutoff, and yet it doesn't affect the integrand in Figure S3 significantly.

From Figure S3, it is clear that for higher multipole transitions, the integrand peaks at values of u far greater than $u = 1$, which is the value associated with the surface plasmon pole (*27*). When this happens, we can approximate the lineshape function in the integrand of Equation (S8) by $\frac{1}{\pi Q u}$. The decay rate (which is in this limit purely nonradiative) is therefore

$$\Gamma_{nr}^{En} = \eta_0 \times \frac{4(2n-1)!\alpha\omega_0}{(m_e c)^2(\epsilon_r + 1)Q}(2kz_0)^{-(2+2(n-1))}C_n. \tag{S9}$$

We can thus see that the decay rate is a purely increasing function of η_0. In fact, once non-radiative decay becomes unimportant, the decay rate transitions from increasing with η_0 to increasing as $\eta_0^{3+2(n-1)}$. We conclude therefore that higher confinement is always beneficial to achieving increasing decay rates.

We conclude this section by noting that for the parameters that we investigated, emission

into SPs tends to be the dominant contribution to the decay rate for dipole transitions. Thus, for investigations into two-plasmon spontaneous emission mediated by dipole transitions and singlet-triplet transitions, one is often justified in using lossless QED based on mode expansion. That said, we will consider this process with losses included.

3.2 Spin Flip Magnetic Multipole (Mn) Transitions

In this section, we derive the rate at which an excited state flips its spin due to vacuum fluctuations in the magnetic field. We look at both radiative and non-radiative decays into 2D plasmons as a function of their confinement factor. The part of the Hamiltonian governing this behavior is $\frac{e\hbar}{2m_e}\boldsymbol{\sigma}\cdot\mathbf{B}$ (48). The magnetic field operator is given by

$$B_i(\mathbf{r}) = (\nabla \times \mathbf{A})_i = \sqrt{\frac{\hbar}{\pi\epsilon_0}} \int d\omega' \frac{\omega'}{c^2} \int d\mathbf{r}' \sqrt{\text{Im }\epsilon(\mathbf{r}',\omega')} \varepsilon_{ilm}\partial_l G_{mj}(\mathbf{r},\mathbf{r}';\omega')\hat{f}_j(\mathbf{r}',\omega') + \text{H.c.},$$
(S10)

where ϵ_{ilm} is the Levi-Civita symbol, and ∂_l is a shorthand for $\frac{\partial}{\partial x_l}$. Applying the Fermi Golden Rule in a manner similar to that in Section II, the decay rate is given by:

$$\Gamma = \frac{2\pi}{\hbar^2}\frac{e^2\hbar^3}{4\pi\epsilon_0 m_e^2 c^2}\sigma_i^{eg}\sigma_r^{*eg}\int\int d\mathbf{r}d\mathbf{r}'\,\psi_g^*(\mathbf{r})\psi_g(\mathbf{r})\left[\text{Im }\varepsilon_{ilm}\varepsilon_{rst}\partial_l\partial_s' G_{mt}(\mathbf{r},\mathbf{r}',\omega_0)\right]\psi_e(\mathbf{r})\psi_e^*(\mathbf{r}'),$$

where σ_k^{eg} denotes the k-th component of the overlap of the spin part of the excited and ground states, and ∂' denotes partial derivatives with respect to $\mathbf{r}'$. Simplifying further, the decay rate is given by:

$$\Gamma = -\frac{e^2\hbar}{4\epsilon_0 m_e^2 c^2}\text{Re}\left[\frac{1}{(2\pi)^2}\int d\mathbf{q}\,M_i M_r^- \varepsilon_{ilm}\varepsilon_{rst}k_l k_s^-(C_{mt}^s + C_{mt}^p)\right],$$

where: $k = (\mathbf{q}, k_\perp), k^- = (-\mathbf{q}, k_\perp), \mathbf{M} = \boldsymbol{\sigma}^{eg}\int d\mathbf{r}\psi_g e^{i\mathbf{q}\cdot\boldsymbol{\rho}+ik_\perp z}\psi_e$ and $\mathbf{M}^- = \boldsymbol{\sigma}^{eg*}\int d\mathbf{r}\psi_g e^{-i\mathbf{q}\cdot\boldsymbol{\rho}+ik_\perp z}\psi_e$. Once again, we consider only the p-polarized contribution in the electrostatic limit. This further simplifies to

$$\Gamma = \frac{\alpha\omega_0}{2(\epsilon_r+1)}\left(\frac{\hbar\omega_0}{m_e c^2}\right)^2\eta_0\int d\theta du\, e^{-2\eta_0 k z_0 u}|\langle g|\sigma_\perp e^{-i\mathbf{q}\cdot\boldsymbol{\rho}-q(z-z_0)}|e\rangle|^2\left(\frac{1}{\pi}\frac{\frac{\sigma_R u}{\sigma_I}}{\left(\frac{\sigma_R u}{\sigma_I}\right)^2 + (1-u)^2}\right),$$
(S11)

For a transition with a change in orbital angular momentum of $(n-1)$ (an Mn transition), the matrix elements in Equation (S21) can be expressed as $C_n \eta_0^{2(n-1)} u^{2(n-1)}$ (the C_n here is not the same as that discussed in the section on electric multipole transitions). When the change in the z-projected orbital angular momentum is zero, the radiative and non-radiative decay rates are respectively:

$$\Gamma_r^{Mn} = \eta_0^{1+2(n-1)} \times \frac{\pi \alpha \omega_0}{(\epsilon_r + 1)} \left(\frac{\hbar \omega_0}{m_e c^2} \right)^2 e^{-2\eta_0 k z_0} C_n \tag{S12}$$

and

$$\Gamma_{nr}^M = \eta_0 \frac{(2n-3)! \alpha \omega_0}{Q(\epsilon_r + 1)} \left(\frac{\hbar \omega_0}{m_e c^2} \right)^2 (2k z_0)^{-2(n-1)} C_n \tag{S13}$$

Note that Equation (S13) does not hold for $n = 1$ (magnetic dipole transition). In this case, the formula for the rate is more complicated, and we do not derive it here. We note that the radiative result can again be derived from a canonical quantization scheme, where the $\mathbf{B}$ operator is obtained by taking the curl of the $\mathbf{A}$ operator mentioned at the end of Sec. II (without the electrostatic approximation).

4 Second Order Processes - Intercombination Transitions and Two Plasmon Emission

4.1 Electric Dipole (Intercombination) Mechanism

The rate of the singlet-triplet transition is generally limited by the weakness of the spin-orbit interaction. However, in atoms and molecules near 2D conductors, the rate of the singlet-triplet transition can be greatly enhanced due to the strong enhancement of electric-dipole transitions. For instructional purposes, we consider here a situation in which the ground state is a singlet with no nearly degenerate triplet states, and the excited state is a triplet state, which has nearly degenerate singlet states nearby. In this case, the transition rate from an triplet state $|T_1, 0\rangle$ to a

singlet state $|S_0, \mathbf{q}\rangle$ under the influence of a perturbation $H_{SO} + (\mathbf{d}_1 \cdot \mathbf{E}_1 + \mathbf{d}_2 \cdot \mathbf{E}_2)$ is given by

$$\Gamma = \frac{2\pi}{\hbar^2} \sum_{\mathbf{q}} \Big| \sum_n \frac{\langle S_0, \mathbf{q}|(\mathbf{d}_1 \cdot \mathbf{E}_1(\mathbf{r}_1) + \mathbf{d}_2 \cdot \mathbf{E}_2(\mathbf{r}_2))|S_n, 0\rangle \langle S_n, 0|H_{SO}|T_1, 0\rangle}{E_{T_1} - E_{S_n}} \Big|^2 \delta(\omega(\mathbf{q}) - \omega_0)$$

(S14)

Taking the approximation of one main contributing intermediate singlet state, $|S'\rangle$, the spin-orbit and electromagnetic effects separate as follows:

$$\Gamma = \frac{2\pi}{\hbar^2} \sum_{\mathbf{q}} |\langle S_0, \mathbf{q}|(\mathbf{d}_1 \cdot \mathbf{E}_1(\mathbf{r}_1) + \mathbf{d}_2 \cdot \mathbf{E}_2(\mathbf{r}_2))|S', 0\rangle|^2 \Big| \frac{\langle S_n, 0|H_{SO}|T_1, 0\rangle}{E_{T_1} - E_{S'}} \Big|^2 \delta(\omega(\mathbf{q}) - \omega_0).$$

In Helium-like atoms (and many other atoms and molecules), the spatial parts of singlet and triplet states are well-described by (resp.) antisymmetrized or symmetrized combinations of two single-particle states. Taking two single-particle states $|\alpha\rangle$ and $|\beta\rangle$, we can write spatial wavefunctions such as: $|\alpha\rangle|\beta\rangle + |\beta\rangle|\alpha\rangle$ and $|\alpha\rangle|\gamma\rangle + |\gamma\rangle|\alpha\rangle$ to describe spin-singlets $|S_0\rangle$ and $|S'\rangle$ (As an example, take $\alpha = 2S$ and $\beta = 2S$, $\gamma = 2P$. This example corresponds to a two states in the Helium atom separated by a wavelength of 2.06 μm (*31*)). When considering the Purcell enhancement associated with placing an excited spin-triplet or spin-singlet near plasmons, the same spin-orbit coupling factor shows up as that which shows up in the free-space decay rate. Therefore, the spin-orbit coupling does not show up in the Purcell factor, which we show is given by:

$$F_p^{S \to T} = \eta_0^3 \times \frac{3\pi f}{(\epsilon_r + 1)} e^{-2\eta_0 k z_0} \times \int du \, u^2 e^{-2\eta_0 k z_0(u-1)} \left(\frac{1}{\pi} \frac{\frac{\sigma_R u}{\sigma_I}}{(\frac{\sigma_R u}{\sigma_I})^2 + (1-u)^2} \right), \quad \text{(S15)}$$

where $f = \frac{1}{2}$ if the dipole is oriented parallel to the surface of the conductor, and $f = 1$ if the dipole is oriented perpendicular to the surface. In the lossless limit, the integral over u is one, giving a result in agreement with the well-known η_0^3 decay law for dipolar emitters discussed in the main text.

12

4.2 Two Plasmon Spontaneous Emission

Finally, we consider situations in which an emitter above a 2D conductor can emit two excitations of the electromagnetic field, a process that is second-order in the perturbation theory. We consider an initial state $|e, 0\rangle$ and a final state $|g, \mathbf{r}\omega k, \mathbf{r}'\omega' k\rangle \equiv \hat{f}_k^\dagger(\mathbf{r}, \omega)\hat{f}_{k'}^\dagger(\mathbf{r}', \omega')|g, 0\rangle$. The atom is coupled to the field through a perturbation, V. Fermi's Golden Rule for this decay reads:

$$\Gamma = \frac{2\pi}{\hbar^2}\frac{1}{2}\int d\mathbf{r}d\mathbf{r}' \int d\omega d\omega' \sum_{k,k'} \left|\sum_{i_1} \frac{\langle g, \mathbf{r}\omega k, \mathbf{r}'\omega' k'|V|i_1\rangle\langle i_1|V|e, 0\rangle}{E_e - E_{i_1} + i0^+}\right|^2 \delta(\omega_0 - \omega - \omega'), \quad (S16)$$

where $|i_1\rangle$ are intermediate states containing both the atom and field degrees of freedom. The sum is understood to be a sum over discrete degrees of freedom and an integral over continuous ones. The factor of $1/2$ comes from the fact that when we sum over all $\{\mathbf{r}\omega k, \mathbf{r}'\omega' k\}$ pairs, each pair of excitations appears twice.

For simplicity, we work in the dipole approximation, in which $V = -\mathbf{d} \cdot \mathbf{E}(\mathbf{r_0})$, where $\mathbf{r}_0$ is the atom position which we define as $(0, 0, z_0)$, using the coordinate system in Figure 1 of the main text. The electric-field operator is:

$$\mathbf{E}(\mathbf{r}_0) = i\sqrt{\frac{\hbar}{\pi\epsilon_0}} \int d\omega \frac{\omega^2}{c^2} \int d\mathbf{r}' \sqrt{\text{Im } \epsilon(\mathbf{r}')}\mathbf{G}(\mathbf{r}_0, \mathbf{r}'; \omega) \cdot \hat{\mathbf{f}}(\mathbf{r}', \omega) + \text{H.c.}. \quad (S17)$$

Using the above electric-field operator and the dipole interaction Hamiltonian, the decay rate into two lossy excitations is given by the general formula:

$$\frac{32\pi\alpha^2}{c^2} \int\limits_0^{\omega_0} d\omega\, \omega^2(\omega_0 - \omega)^2 \text{Im } G_{ri}(\mathbf{r}_0, \mathbf{r}_0, \omega)\text{Im } G_{sj}(\mathbf{r}_0, \mathbf{r}_0, \omega_0 - \omega)\times$$

$$\sum_{m,n} \left(\frac{x_j^{gn} x_i^{ne}}{\omega_e - \omega_n - \omega} + \frac{x_i^{gn} x_j^{ne}}{\omega_e - \omega_n - (\omega_0 - \omega)}\right) \left(\frac{x_s^{gm} x_r^{me}}{\omega_e - \omega_m - \omega} + \frac{x_r^{gm} x_s^{me}}{\omega_e - \omega_m - (\omega_0 - \omega)}\right)^*,$$

$$(S18)$$

where $x_i^{ab} \equiv \langle a|\hat{e}_i \cdot \mathbf{r}|b\rangle$. We point out here that in the hydrogen atom, the energy denominators diverge at as $\omega \to 0$, leading to an apparent infrared divergence in the two-photon decay rate.

13

This divergence stems from the degeneracy between the initial state and some intermediate state and is this ultimately regulated by the Lamb shifts, which split the aforementioned degeneracy. Because the Lamb shifts only very weakly modify the eigenfunctions of the coulomb potential, the only effect of the Lamb shift is to renormalize the hydrogen energy levels. This is equivalent to putting a low-frequency cutoff in the integral at $\omega_{LS} \equiv \frac{E_{LS}}{\hbar}$, where E_{LS} is the Lamb shift between the initial state and the once degenerate intermediate state. Below this cutoff, the integrand drops sharply. The Lamb shifts are taken from (*31*). In non-Hydrogenic atom, this issue in general does not arise.

As discussed in Section II, Im G_{ij} can be expressed in terms of the imaginary part of the reflectivity Im r_p and polarization vectors, $\hat{\epsilon}(\theta) = \frac{\hat{\mathbf{q}}+i\hat{\mathbf{z}}}{\sqrt{2}}$, where θ is the angle between $\hat{\mathbf{q}}$ and the x-axis of q-space. Also as discussed in Sec. II, the imaginary part of the reflectivity can be expressed as Im $r_p(u, \omega) = \frac{2\pi}{\epsilon_r+1} \left(\frac{1}{\pi} \frac{u/Q(\omega)}{(1-u)^2+(u/Q(\omega))^2} \right)$, where $u = q/q_0$, with $q_0(\omega) = \frac{(\epsilon_r+1)\omega\epsilon_0}{\text{Im } \sigma(\omega)}$, just as in Sec. II. The lossless limit of the two-excitation spontaneous emission rate per unit frequency (also known as the differential decay rate) is found to be:

$$\frac{d\Gamma}{dy} = \frac{16\pi\omega_0\alpha^2 k^4}{(\epsilon_r+1)^2} \times [y(1-y)\eta(y)\eta(1-y)]^3 \, e^{-2kz_0[y\eta(y)+(1-y)\eta(1-y)]} \times$$
$$\left\langle \left| \sum_n \frac{(\mathbf{r}^{gn} \cdot \hat{\epsilon}(\theta))(\mathbf{r}^{ne} \cdot \hat{\epsilon}(\theta'))}{y_e - y_n - y} + \frac{(\mathbf{r}^{gn} \cdot \hat{\epsilon}(\theta))(\mathbf{r}^{ne} \cdot \hat{\epsilon}(\theta'))}{y_e - y_n - (1-y)} \right|^2 \right\rangle_{\theta,\theta'}, \quad \text{(S19)}$$

where $k = \frac{\omega_0}{c}$ and $\Gamma \equiv \int_0^1 dy \, \frac{d\Gamma}{dy}$. In writing the previous equation, we have performed the non-dimensionalizations: $\eta(y) = \frac{cq(y)}{\omega(y)}$, and $y = \frac{\omega}{\omega_0}^2$ [3] A relatively simple case of this expression occurs when the initial and final states are s states. The intermediate states are then of the form $|i_1\rangle = |np_j\rangle$ for $j = x, y, z$. In the electrostatic limit, $\hat{\epsilon}(\theta) = \frac{\cos(\theta)\hat{\mathbf{x}}+\sin(\theta)\hat{\mathbf{y}}+i\hat{\mathbf{z}}}{\sqrt{2}}$. The angular average is $3/8$ and the differential decay rate can be expressed in terms of matrix elements of z,

---

[2]Although the angular integrals could have already been performed, we express our answer in terms of polarization vectors to make the result take the form of that which would be obtained through canonical quantization using the (lossless) field operators presented at the end of Section 2.

[3]Another useful non-dimensionalization for atomic systems, that allows for quick estimation of the decay rate is $\mathbf{r} \equiv a_0\mathbf{x}$.

$z_{gn} \equiv \langle g|z|n \rangle$, as:

$$\frac{6\pi\omega_0\alpha^2 k^4}{(\epsilon_r + 1)^2} \times [y(1-y)\eta(y)\eta(1-y)]^3 e^{-2kz_0[y\eta(y)+(1-y)\eta(1-y)]} \times$$

$$\left| \sum_n z_{gn} z_{ne} \left(\frac{1}{y_e - y_n + y - 1} + \frac{1}{y_e - y_n - y} \right) \right|^2.$$

The two-photon differential emission rate in free-space, by comparison is (*51,55*)

$$\frac{4}{3\pi}\alpha^2 k^4 y^3 (1-y)^3 \left| \sum_n z_{gn} z_{ne} \left(\frac{1}{y_e - y_n + y - 1} + \frac{1}{y_e - y_n - y} \right) \right|^2.$$

Therefore, the enhancement factor per unit frequency in free-space is

$$\frac{d\Gamma/dy\big|_{pl}}{d\Gamma/dy\big|_{fs}} = \frac{9\pi^2}{2(\epsilon_r + 1)^2}\eta^3(y)\eta^3(1-y)e^{-2kz_0[y\eta(y)+(1-y)\eta(1-y)]}. \tag{S20}$$

Equation (S20) can be re-expressed in terms of the Purcell factor, $F_p(\omega)$, for the single plasmon emission of a dipole polarized perpendicular to the 2D conductor as

$$\frac{d\Gamma/dy\big|_{pl}}{d\Gamma/dy\big|_{fs}} = \frac{1}{2}F_p(y)F_p(1-y). \tag{S21}$$

Equation (S21) also holds when plasmon losses are taken into account, as we show below.

4.2.1 Effect of Dispersion on Lossless Rates

In the main text, we use the Drude dispersion in order to evaluate the two-plasmon spontaneous emission rate. In the Drude model, the dispersion relation implies that $\eta(y) = \frac{\omega c}{\beta^2} = \frac{\omega_0 c}{\beta^2}y$, where β is a constant determined by the plasma frequency and thickness of the metal. We define the characteristic squeezing $\eta_0 = \frac{\omega_0 c}{2\beta^2}$. The factor of 2 in the definition of η_0 is natural because most of the emission comes from frequencies near $\omega = \frac{\omega_0}{2}$. It thus follows that the differential decay rate is:

$$\frac{d\Gamma}{dy}\bigg|_{Drude} = 384\frac{\pi\omega_0}{(\epsilon_r + 1)^2}\alpha^2 k^4 \eta_0^6 y^6 (1-y)^6 e^{-4\eta_0 kz_0(y^2+(1-y)^2)}\left| \sum_n z_{gn} z_{ne} \left(\frac{1}{y_e - y_n + y - 1} + \frac{1}{y_e - y_n - y} \right) \right|^2 \tag{S22}$$

In many cases, the 2D plasmon dispersion is approximately linear with wavevector, i.e., $\eta(y) = \eta_0$, where η_0 is some constant squeezing that can be as high as 360 (in Beryllium for example). Values of 240 have been observed in graphene (*11–13*). Therefore, the differential decay rate is (in the low loss limit):

$$\frac{d\Gamma}{dy}\bigg|_{\text{const } \eta} = \frac{6\pi\omega_0}{(\epsilon_r + 1)^2}\alpha^2 k^4 \eta_0^6 y^3 (1-y)^3 e^{-4\eta_0 k z_0}\left|\sum_n z_{gn}z_{ne}\left(\frac{1}{y_e - y_n + y - 1} + \frac{1}{y_e - y_n - y}\right)\right|^2 \tag{S23}$$

4.2.2 The Effect of Losses on Two Plasmon Spontaneous Emission

In this section, we estimate the effect of losses on the two-excitation spontaneous emission rate and show that the lossless decay rates computed in the main text are generally not significantly altered by losses. For simplicity, we consider transitions between S states, although our calculations can straightforwardly be generalized to other transitions. To compute emission of two excitations in the presence of dissipation, the starting point is Equation (S18). The decay rate can be expressed as

$$\frac{6\pi\alpha^2 c^2}{(\epsilon_r + 1)^2}\int_0^{\omega_0} d\omega\,\omega^2(\omega_0 - \omega)^2 I(\omega)I(\omega_0 - \omega)\left|\sum_n z_{gn}z_{ne}\left(\frac{1}{y_e - y_n + y - 1} + \frac{1}{y_e - y_n - y}\right)\right|^2, \tag{S24}$$

in which $I(\omega)$ is a shorthand for

$$q_0^3(\omega)e^{-2q_0(\omega)z_0}\int du\,u^2 e^{-2qz_0(u-1)}\left(\frac{1}{\pi}\frac{u/Q(\omega)}{(1-u)^2 + (u/Q(\omega))^2}\right) \equiv q_0^3(\omega)e^{-2q_0(\omega)z_0}I(u,\omega). \tag{S25}$$

In the lossless limit, the integral evaluates to 1, reproducing the lossless result, as expected. It can thus be seen that the ratio of the total differential decay rate to the lossless differential decay

16

rate is

$$\frac{d\Gamma_{TOT}/dy}{d\Gamma_r/dy} = \left[\int du\, u^2 e^{-2q_0(y)z_0(u-1)} \left(\frac{1}{\pi} \frac{u/Q(y)}{(1-u)^2 + (u/Q(y))^2} \right) \right] \times$$
$$\left[\int du\, u^2 e^{-2q_0(1-y)z_0(u-1)} \left(\frac{1}{\pi} \frac{u/Q(1-y)}{(1-u)^2 + (u/Q(1-y))^2} \right) \right] \qquad \text{(S26)}$$

Equation (S26), in combination with Equation (S8) demonstrate that for $S \to S$ transitions, the differential decay rate enhancement is still $\frac{1}{2}F_p(y)F_p(1-y)$. In Fig. S4, we compare the differential decay rates with losses to those without losses for atom-surface separations of 0.5, 1, 5, and 15 nm. The transition under consideration is the $4s \to 3s$ transition in Hydrogen, just as in the main text. The model assumed to hold through the entire decay spectrum is the Drude model, in which $Q(\omega) = \omega\tau \implies Q(y) = (\omega_0\tau)y$, where τ is the frequency-independent relaxation time. Although a more realistic model for the conductivity can be adopted, we choose the Drude model for instructional purposes. In the simulations resulting in Fig. S4, we chose the confinement factor at $y = 0.5$ to be 150, just as in the main text. We also chose the quality factor at $y = 0.5$ to be 20. We can see that for distances between 5 and 15 nm, the decay is mostly through plasmons. However, for distances below 1 nm, we can see two phenomena. The first being that the dominant mode of decay is through the loss mechanisms that determine the relaxation time. The second is that the peak of the emission is no longer at $y = 0.5$. From these last two observations, we arrive at two conclusions. The first is that at short atom-surface separations, entangled lossy excitations (such as particle-hole excitations or phonons) can be produced at high rates. The second is that the spectral shape of an emitter can be significantly altered by the presence of losses.

To conclude our discussion of losses and two-plasmon emission, we present analytical (up to atomic matrix elements) expressions for the differential decay rate when non-radiative decay is a dominant effect. What can be computed exactly and analytically is the ratio of this differential decay rate to the free-space differential decay rate. At short distances, or long wavelengths, i.e;

17

$q(\omega_0)z_0 \ll 1$, and for $Q \gg 1$ (in practice, Q = 3 can already be high enough), each of the integrals in Equation (S24) becomes

$$\frac{1}{\pi Q(\omega)} e^{2q_0(\omega)z_0} (2q_0(\omega)z_0)^{-2},$$

where $\omega = \omega_0 y$ or $\omega_0(1-y)$. When this happens, the differential decay rate becomes:

$$\frac{d\Gamma}{dy}\bigg|_{\text{Lossy}} = \frac{3\omega_0\alpha^2}{8\pi(\epsilon_r + 1)^2} \frac{1}{z_0^4} \times \left[\frac{y(1-y)\eta(y)\eta(1-y)}{Q(y)Q(1-y)}\right] \times$$
$$\left|\sum_n z_{gn}z_{ne}\left(\frac{1}{y_e - y_n + y - 1} + \frac{1}{y_e - y_n - y}\right)\right|^2.$$
(S27)

When $Q \ll 1$, one of the two integrals in Equation (S24) becomes linear in Q. The enhancement of the differential decay rate is given by the previous equation divided by the free-space differential emission rate and is independent of atomic parameters. The analysis of this section can be generalized to arbitrary dispersion relations such as Drude or linear.

Finally, a word of caution about the use of these estimates: when z_0 approaches the emitter size, the dimensionless decay rate approaches 1, indicating the necessity of including nonlocality and potentially the breakdown of perturbative quantum electrodynamics. Therefore, these formulas should not be used in those short-distance cases, but rather should be used to estimate the distance at which nonlocality is important and at which perturbation theory breaks down.

5   Experimental Signatures of Forbidden Transitions

We briefly discuss a potential scheme by which to observe forbidden transitions (like the ones described in this paper) through radiative cascade in a four-level system like that illustrated in Figure S5. The assumptions regarding the levels are noted in Figure S5. Electrons in this emitter are excited to level 1 by usual means (electrically or through a far-field photon). If a forbidden transition does not occur, the possible transitions may be $1 \to 0$ or $1 \to 3$. If a forbidden transition from $1 \to 2$ occurs, then a far-field photon emission can occur from $2 \to 3$ if this

transition is at a high enough frequency to be insignificantly enhanced by plasmons, or if it is in the cutoff region of graphene. The observation of a photon at this frequency is already a qualitative signal of forbidden transitions taking place. Combined with quantitative understanding of the intensity of far-field photon emission from $2 \to 3$ as a function of atom-surface separation and confinement factor (which can be electrostatically controlled in graphene), the exact type of forbidden-transition can be inferred. This is because, as we have shown in the text, every type of forbidden transition has different dependences on confinement and atom-surface separation.

This finding points to a way of reshaping the far-field spectrum of emitter, even without outcoupling any excitations. Therefore, even with very high losses which may seem overcomeable, an interesting application of these highly confined plasmons emerges naturally.

6   Summary of Results

In this section, we summarize our results for the various decay rates in purely radiative and purely non-radiative limits. For electric (En) transitions, the radiative decay rate is:

$$\Gamma_r^{En} = \eta_0^{3+2(n-1)} \times \frac{4\pi\alpha^3\omega_0}{(\epsilon_r + 1)} e^{-2\eta_0 kz_0} C_n.$$

The corresponding non-radiative decay rate is:

$$\Gamma_{nr}^{En} = \eta_0 \times \frac{4(2n-1)!\alpha^3\omega_0}{(\epsilon_r + 1)Q}(2kz_0)^{-(2+2(n-1))} C_n.$$

For spin flip transitions, the radiative decay rate is:

$$\Gamma_r^{Mn} = \eta_0^{1+2(n-1)} \times \frac{\pi\alpha\omega_0}{(\epsilon_r + 1)} \left(\frac{\hbar\omega_0}{m_e c^2}\right)^2 e^{-2\eta_0 kz_0} C_n.$$

The corresponding non-radiative decay rate is (for $n \neq 1$):

$$\Gamma_{nr}^{Mn} = \eta_0 \times (2n-3)!\frac{\alpha\omega_0}{Q(\epsilon_r + 1)} \left(\frac{\hbar\omega_0}{m_e c^2}\right)^2 (2kz_0)^{-2(n-1)} C_n.$$

For intercombination transitions in the single-contributing intermediate state approximation, the Purcell factor in the lossless limit is

$$F_p^{S \leftrightarrow T} = \frac{3\pi f}{\epsilon_r + 1} \eta_0^3 e^{-2\eta_0 k z_0}$$

For two-plasmon spontaneous emission, the second order differential purcell-factor within the dipole approximation is:

$$\frac{d\Gamma/dy\big|_{pl}}{d\Gamma/dy\big|_{fs}} = \eta_0^6 \times 72\pi^2 (e^{-4\eta_0 k z_0})(y - y^2)^3 e^{8\eta_0 k z_0 y(1-y)},$$

which can be recast into the remarkably simple form:

$$\frac{d\Gamma/dy\big|_{pl}}{d\Gamma/dy\big|_{fs}} = \frac{1}{2} F_p(y) F_p(1 - y),$$

which holds even when losses are present (although then the decay is not purely into plasmons).
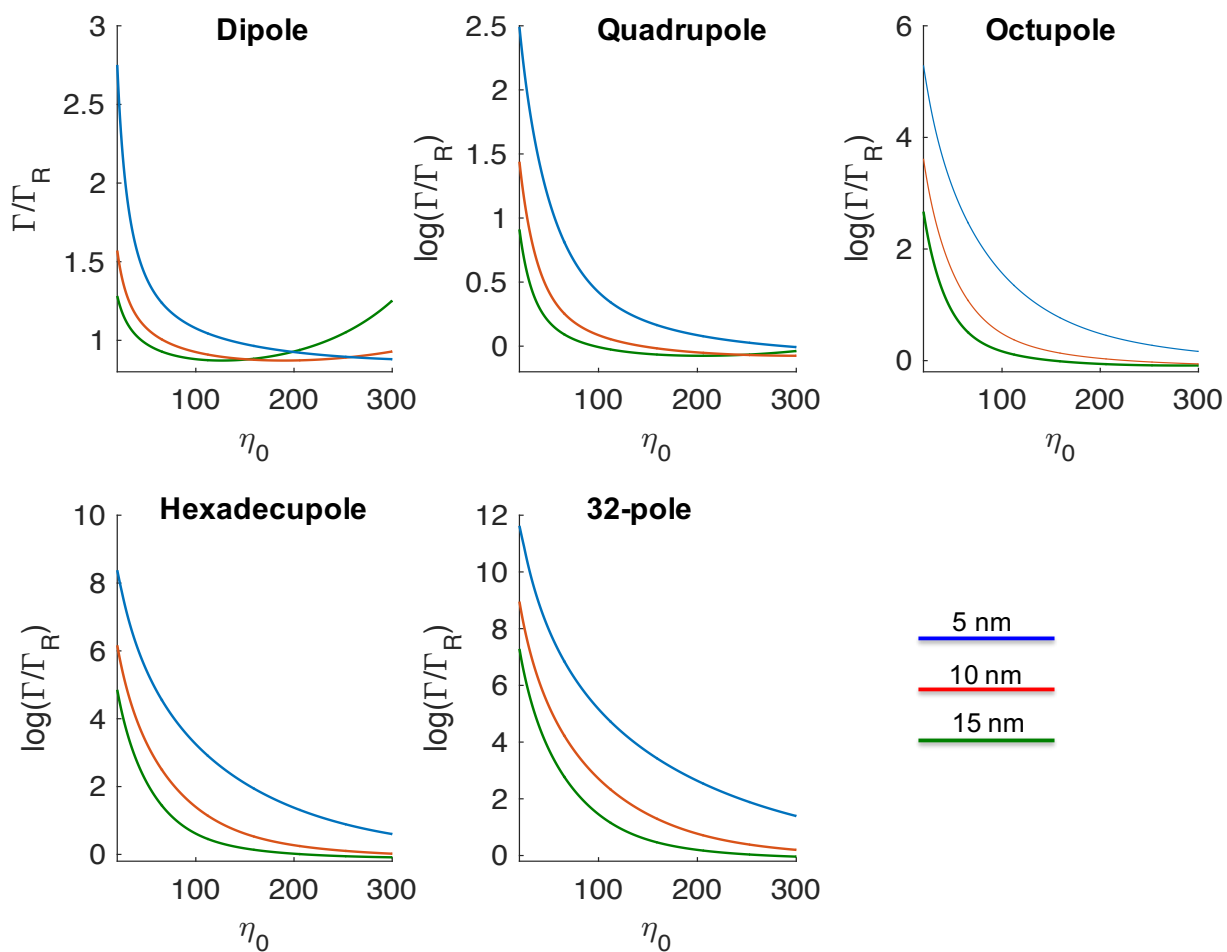
Figure S2: **Ratio of total decay rate to decay rate into plasmons - Multipolarity and Confinement Dependence**: plotted as a function of on-resonance confinement factor η_0 at different atom-surface separations for E(1-5) transitions in the Hydrogen 6↔5 transition series. The minimum confinement factor considered in this figure is 20.
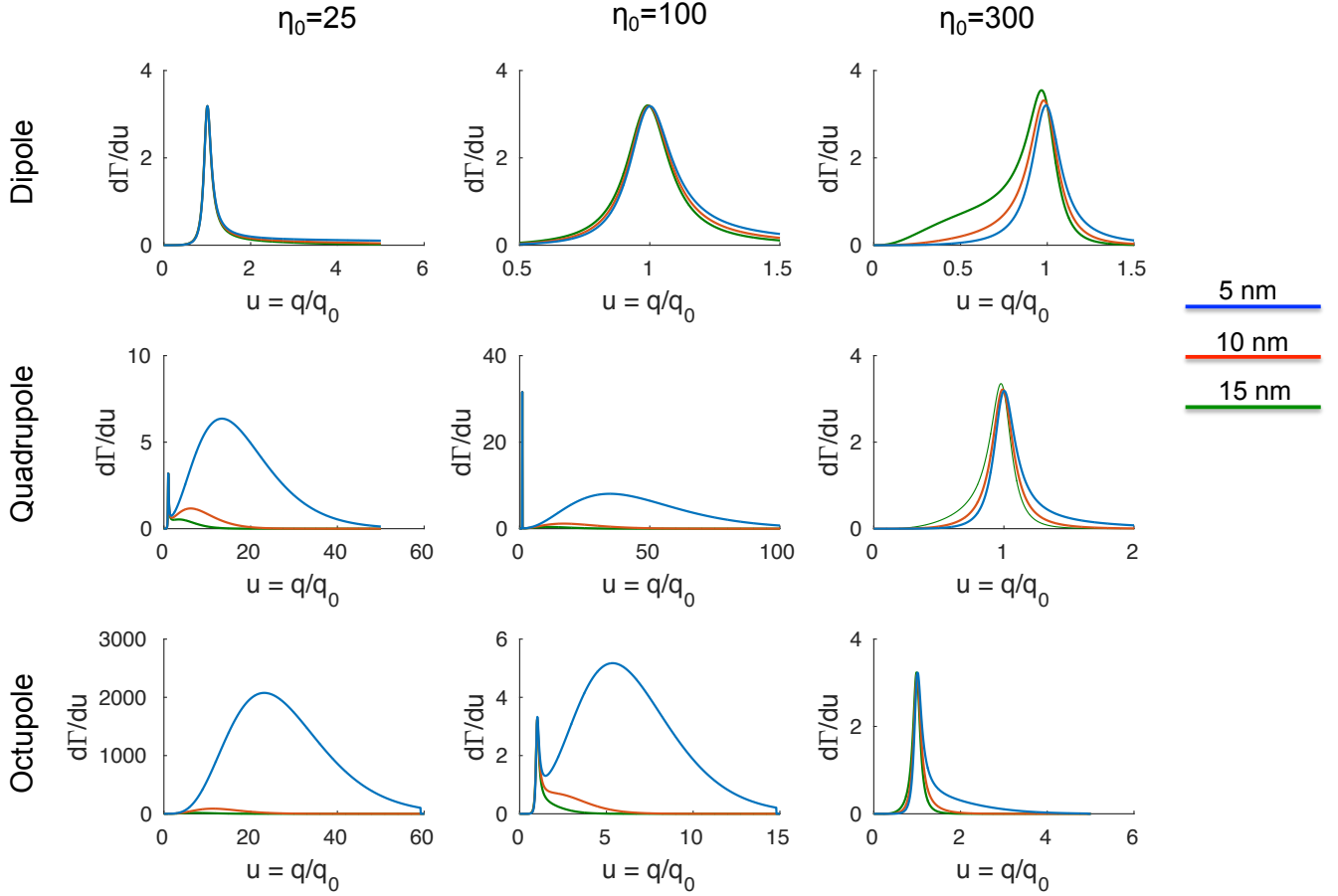
Figure S3: **Effect of Confinement and Multipolarity on Radiative and Non-Radiative Decay Rates**: Integrand of Eq. (S8) (normalized to Γ_R) plotted for dipole (top), quadrupole (middle), and octupole (bottom) transitions at three different on-resonance confinements ($\eta_0 = \{25, 100, 300\}$) and atom-surface separations ($z_0 = \{5 \text{ nm}, 10 \text{ nm}, 15 \text{ nm}\}$).
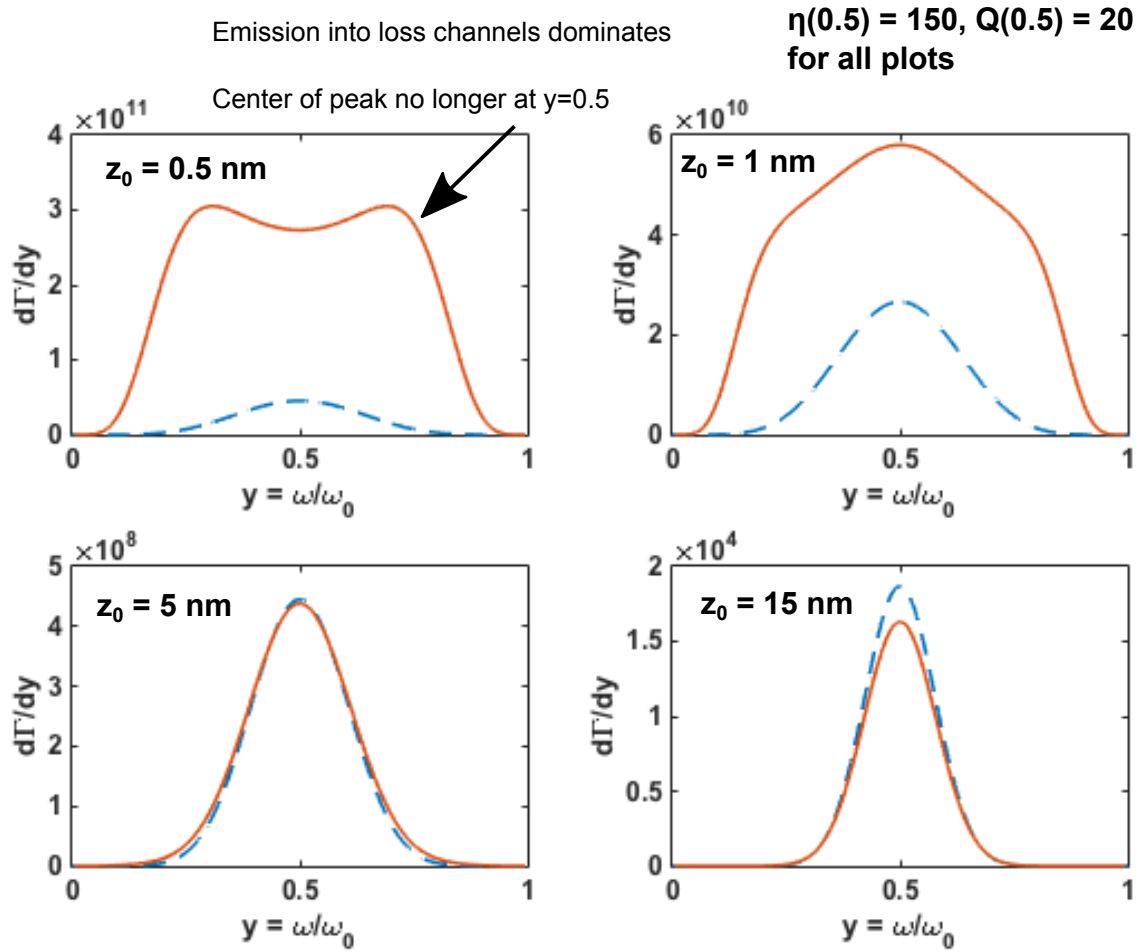
Figure S4: **Effect of Losses on Two Plasmon Spontaneous Emission**: Differential decay rate $d\Gamma/dy$ plotted as a function of y for lossless (dashed blue) and lossy (solid orange) 2D conductors. A Drude model to describe Graphene is assumed. The lossless version of these differential decay plots are plotted for the same transition as Fig. 4b in the main text.
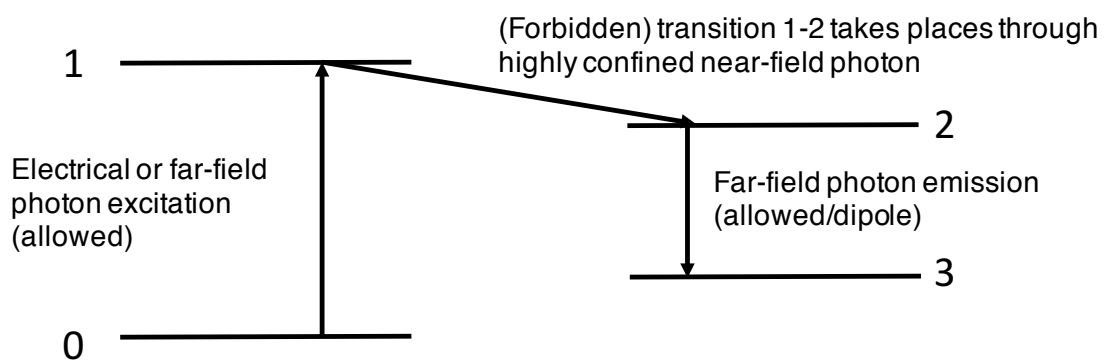
Figure S5: **Detecting forbidden transitions indirectly via radiative cascade.** Schematic four-level system by which the presence of forbidden transitions can be inferred. It is assumed that $0 \rightarrow 1$ is allowed, $1 \rightarrow 2$ is forbidden, and $2 \rightarrow 3$ is allowed and occurs non-negligibly through far-field photon emission.

References and Notes

1. P. A. Dirac, The quantum theory of the emission and absorption of radiation. *Proc. R. Soc. London Ser. A* **114**, 243–265 (1927). doi:10.1098/rspa.1927.0039

2. M. Pelton, Modified spontaneous emission in nanophotonic structures. *Nat. Photonics* **9**, 427–435 (2015). doi:10.1038/nphoton.2015.103

3. M. Tame, K. R. McEnery, Ş. K. Özdemir, J. Lee, S. A. Maier, M. S. Kim, Quantum plasmonics. *Nat. Phys.* **9**, 329–340 (2013). doi:10.1038/nphys2615

4. R. Friend, R. W. Gymer, A. B. Holmes, J. H. Burroughes, R. N. Marks, C. Taliani, D. D. C. Bradley, D. A. D. Santos, J. L. Brdas, M. Lgdlund, W. R. Salaneck, *Nature* **397**, 121–128 (1999). doi:10.1038/16393

5. A. Köhler, H. Bässler, Triplet states in organic semiconductors. *Mater. Sci. Eng. Rep.* **66**, 71–109 (2009). doi:10.1016/j.mser.2009.09.001

6. M. Göppert, Über die Wahrscheinlichkeit des Zusammenwirkens zweier Lichtquanten in einem Elementarakt. *Naturwissenschaften* **17**, 932 (1929). doi:10.1007/BF01506585

7. C. L. Cesar, D. G. Fried, T. C. Killian, A. D. Polcyn, J. C. Sandberg, I. A. Yu, T. J. Greytak, D. Kleppner, J. M. Doyle, Two-photon spectroscopy of trapped atomic hydrogen. *Phys. Rev. Lett.* **77**, 255–258 (1996). Medline doi:10.1103/PhysRevLett.77.255

8. A. Hayat, P. Ginzburg, M. Orenstein, Observation of two-photon emission from semiconductors. *Nat. Photonics* **2**, 238–241 (2008). doi:10.1038/nphoton.2008.28

9. A. Nevet, N. Berkovitch, A. Hayat, P. Ginzburg, S. Ginzach, O. Sorias, M. Orenstein, Plasmonic nanoantennas for broad-band enhancement of two-photon emission from semiconductors. *Nano Lett.* **10**, 1848–1852 (2010). Medline doi:10.1021/nl1005806

10. A. Hayat, A. Nevet, P. Ginzburg, M. Orenstein, Applications of two-photon processes in semiconductor photonic devices. *Semicond. Sci. Technol.* **26**, 083001 (2011). doi:10.1088/0268-1242/26/8/083001

11. T. Nagao, T. Hildebrandt, M. Henzler, S. Hasegawa, Dispersion and damping of a two-dimensional plasmon in a metallic surface-state band. *Phys. Rev. Lett.* **86**, 5747–5750 (2001). Medline doi:10.1103/PhysRevLett.86.5747

12. B. Diaconescu, K. Pohl, L. Vattuone, L. Savio, P. Hofmann, V. M. Silkin, J. M. Pitarke, E. V. Chulkov, P. M. Echenique, D. Farías, M. Rocca, Low-energy acoustic plasmons at metal surfaces. *Nature* **448**, 57–59 (2007). Medline doi:10.1038/nature05975

13. Y. Liu, R. Willis, K. Emtsev, T. Seyller, Plasmon dispersion and damping in electrically isolated two-dimensional charge sheets. *Phys. Rev. B* **78**, 201403 (2008). doi:10.1103/PhysRevB.78.201403

14. E. Rugeramigabo, T. Nagao, H. Pfnür, Experimental investigation of two-dimensional plasmons in a DySi$_2$ monolayer on Si(111). *Phys. Rev. B* **78**, 155402 (2008). doi:10.1103/PhysRevB.78.155402

15. M. Jablan, H. Buljan, M. Soljačić, Plasmonics in graphene at infrared frequencies. *Phys. Rev. B* **80**, 245435 (2009). doi:10.1103/PhysRevB.80.245435

16. S. J. Park, R. E. Palmer, Acoustic plasmon on the Au(111) surface. *Phys. Rev. Lett.* **105**, 016801 (2010). Medline doi:10.1103/PhysRevLett.105.016801

17. A. Grigorenko, M. Polini, K. Novoselov, Graphene plasmonics. *Nat. Photonics* **6**, 749–758 (2012). doi:10.1038/nphoton.2012.262

18. Z. Fei, A. S. Rodin, G. O. Andreev, W. Bao, A. S. McLeod, M. Wagner, L. M. Zhang, Z. Zhao, M. Thiemens, G. Dominguez, M. M. Fogler, A. H. Castro Neto, C. N. Lau, F. Keilmann, D. N. Basov, Gate-tuning of graphene plasmons revealed by infrared nano-imaging. *Nature* **487**, 82–85 (2012). Medline

19. M. Jablan, M. Soljačić, H. Buljan, Plasmons in graphene: Fundamental properties and potential applications. *Proc. IEEE* **101**, 1689–1704 (2013). doi:10.1109/JPROC.2013.2260115

20. K. Tielrooij, L. Orona, A. Ferrier, M. Badioli, G. Navickaite, S. Coop, S. Nanot, B. Kalinic, T. Cesca, L. Gaudreau, Q. Ma, A. Centeno, A. Pesquera, A. Zurutuza, H. de Riedmatten, P. Goldner, F. J. García de Abajo, P. Jarillo-Herrero, F. H. L. Koppens, Electrical control of optical emitter relaxation pathways enabled by graphene. *Nat. Phys.* **11**, 281–287 (2015). doi:10.1038/nphys3204

21. A. Woessner, M. B. Lundeberg, Y. Gao, A. Principi, P. Alonso-González, M. Carrega, K. Watanabe, T. Taniguchi, G. Vignale, M. Polini, J. Hone, R. Hillenbrand, F. H. Koppens, Highly confined low-loss plasmons in graphene-boron nitride heterostructures. *Nat. Mater.* **14**, 421–425 (2015). Medline doi:10.1038/nmat4169

22. Q. Zhang, X. Li, M. M. Hossain, Y. Xue, J. Zhang, J. Song, J. Liu, M. D. Turner, S. Fan, Q. Bao, M. Gu, Graphene surface plasmons at the near-infrared optical regime. *Sci. Rep.* **4**, 6559 (2014). doi:10.1038/srep06559

23. Z. Fei, G. O. Andreev, W. Bao, L. M. Zhang, A. S. McLeod, C. Wang, M. K. Stewart, Z. Zhao, G. Dominguez, M. Thiemens, M. M. Fogler, M. J. Tauber, A. H. Castro-Neto, C. N. Lau, F. Keilmann, D. N. Basov, Infrared nanoscopy of dirac plasmons at the graphene-SiO$_2$ interface. *Nano Lett.* **11**, 4701–4705 (2011). Medline [doi:10.1021/nl202362d](doi:10.1021/nl202362d)

24. H. Yan, T. Low, W. Zhu, Y. Wu, M. Freitag, X. Li, F. Guinea, P. Avouris, F. Xia, Damping pathways of mid-infrared plasmons in graphene nanostructures. *Nat. Photonics* **7**, 394–399 (2013). doi:10.1038/nphoton.2013.57

25. E. Altewischer, M. P. van Exter, J. P. Woerdman, Plasmon-assisted transmission of entangled photons. *Nature* **418**, 304–306 (2002). [Medline](#) [doi:10.1038/nature00869](#)

26. A. Archambault, F. Marquier, J.-J. Greffet, C. Arnold, Quantum theory of spontaneous and stimulated emission of surface plasmons. *Phys. Rev. B* **82**, 035411 (2010). [doi:10.1103/PhysRevB.82.035411](#)

27. F. H. Koppens, D. E. Chang, F. J. García de Abajo, Graphene plasmonics: A platform for strong light-matter interactions. *Nano Lett.* **11**, 3370–3377 (2011). [Medline](#) [doi:10.1021/nl201771h](#)

28. L. Gaudreau, K. J. Tielrooij, G. E. Prawiroatmodjo, J. Osmond, F. J. García de Abajo, F. H. Koppens, Universal distance-scaling of nonradiative energy transfer to graphene. *Nano Lett.* **13**, 2030–2035 (2013). [Medline](#) [doi:10.1021/nl400176b](#)

29. See supplementary materials on *Science* Online.

30. We expect nonlocal effects to kick in at atom-surface separations $z_0 \leq v_f/\omega_0$, where v_f is the Fermi velocity and ω_0 is the transition frequency.

31. A. Kramida *et al.*, Atomic Spectra Database (National Institute of Standards and Technology, Gaithersburg, MD, 2012).

32. J. R. Zurita-Sánchez, L. Novotny, Multipolar interband absorption in a semiconductor quantum dot I: Electric quadrupole enhancement. *J. Opt. Soc. Am. B* **19**, 1355 (2002). [doi:10.1364/JOSAB.19.001355](#)

33. J. R. Zurita-Sánchez, L. Novotny, Multipolar interband absorption in a semiconductor quantum dot II: Magnetic dipole enhancement. *J. Opt. Soc. Am. B* **19**, 2722 (2002). [doi:10.1364/JOSAB.19.002722](#)

34. R. Filter, S. Mühlig, T. Eichelkraut, C. Rockstuhl, F. Lederer, Controlling the dynamics of quantum mechanical systems sustaining dipole-forbidden transitions via optical nanoantennas. *Phys. Rev. B* **86**, 035404 (2012). [doi:10.1103/PhysRevB.86.035404](#)

35. M. Takase, H. Ajiki, Y. Mizumoto, K. Komeda, M. Nara, H. Nabika, S. Yasuda, H. Ishihara, K. Murakoshi, Selection-rule breakdown in plasmon-induced electronic excitation of an isolated single-walled carbon nanotube. *Nat. Photonics* **7**, 550–554 (2013). [doi:10.1038/nphoton.2013.129](#)

36. V. Yannopapas, E. Paspalakis, Giant enhancement of dipole-forbidden transitions via lattices of plasmonic nanoparticles. *J. Mod. Opt.* **62**, 1435–1441 (2015). [doi:10.1080/09500340.2015.1045435](#)

37. M. L. Andersen, S. Stobbe, A. S. Sørensen, P. Lodahl, Strongly modified plasmon–matter interaction with mesoscopic quantum emitters. *Nat. Phys.* **7**, 215–218 (2011). [doi:10.1038/nphys1870](#)

38. I. D. Rukhlenko, D. Handapangoda, M. Premaratne, A. V. Fedorov, A. V. Baranov, C. Jagadish, Spontaneous emission of guided polaritons by quantum dot coupled to metallic nanowire: Beyond the dipole approximation. *Opt. Express* **17**, 17570–17581 (2009). Medline doi:10.1364/OE.17.017570

39. P. K. Jain, D. Ghosh, R. Baer, E. Rabani, A. P. Alivisatos, Near-field manipulation of spectroscopic selection rules on the nanoscale. *Proc. Natl. Acad. Sci. U.S.A.* **109**, 8016–8019 (2012). Medline doi:10.1073/pnas.1121319109

40. G. M. Akselrod *et al.*, *Nat. Photonics* (2014).

41. Technically, $\nabla \cdot \mathbf{E} \neq 0$ only at the surface, but the contribution is small because the atomic wave functions are exponentially suppressed at the surface, so for parameters of interest, the direct s $\rightarrow$ s transition is much weaker than the two-plasmon process.

42. A. F. Page, F. Ballout, O. Hess, J. M. Hamm, Nonequilibrium plasmons with gain in graphene. *Phys. Rev. B* **91**, 075404 (2015). doi:10.1103/PhysRevB.91.075404

43. A. Alabastri, X. Yang, A. Manjavacas, H. O. Everitt, P. Nordlander, Extraordinary light-induced local angular momentum near metallic nanoparticles. *ACS Nano* **10**, 4835–4846 (2016). Medline doi:10.1021/acsnano.6b01851

44. G. Liu, Y. Wu, Y. M. Lin, D. B. Farmer, J. A. Ott, J. Bruley, A. Grill, P. Avouris, D. Pfeiffer, A. A. Balandin, C. Dimitrakopoulos, Epitaxial graphene nanoribbon array fabrication using BCP-assisted nanolithography. *ACS Nano* **6**, 6786–6792 (2012). Medline doi:10.1021/nn301515a

45. A. N. Abbas, G. Liu, B. Liu, L. Zhang, H. Liu, D. Ohlberg, W. Wu, C. Zhou, Patterning, characterization, and chemical sensing applications of graphene nanoribbon arrays down to 5 nm using helium ion beam lithography. *ACS Nano* **8**, 1538–1546 (2014). Medline doi:10.1021/nn405759v

46. T. B. Hoang, G. M. Akselrod, C. Argyropoulos, J. Huang, D. R. Smith, M. H. Mikkelsen, Ultrafast spontaneous emission source using plasmonic nanoantennas. *Nat. Commun.* **6**, 7788 (2015). doi:10.1038/ncomms8788

47. For applications in which fast nonradiative decay is desired, we note that for considerably low wavelengths $1/kz_0 \approx 1$, the nonradiative decay is much faster than one would naively expect. This is because the nonradiative decay still couples to the multipole moment relevant to the atomic transition. Therefore, the strong enhancement of rates coming from matching the atomic size to the wavelength of light compensates for the suppression of rates coming from a higher kz_0. In fact, the total rate—even when nonradiative energy transfer is dominant—increases as the wavelength shrinks. From this, we conclude that for both radiative and nonradiative decay, the high confinement of 2D plasmons helps to overcome the small size of the atom.

48. C. Cohen-Tannoudji, J. Dupont-Roc, G. Grynberg, P. Thickstun, *Atom-Photon Interactions: Basic Processes and Applications* (Wiley, 1992).

49. We note that in principle the spectra increase for low frequencies because of quenching, but in the cases presented, it only provides a weak logarithmic correction to the decay rates (one to two orders of magnitude below the computed decay rates in Fig. 4F). This logarithmic correction is regulated by the energy difference between 4s and 4p levels (due to the Lamb shift). In other atoms, it is regulated by a much larger frequency (due to the lack of degeneracy between s and p orbitals), making the correction even weaker than in hydrogen (*29*).

50. A. Alù, N. Engheta, Tuning the scattering response of optical nanoantennas with nanocircuit loads. *Nat. Photonics* **2**, 307–310 (2008). doi:10.1038/nphoton.2008.53

51. G. Breit, E. Teller, Metastability of hydrogen and helium levels. *Astrophys. J.* **91**, 215 (1940). doi:10.1086/144158

52. L. Knöll, S. Scheel, D.-G. Welsch, QED in dispersing and absorbing media. In *Coherence and Statistics of Photons and Atoms*, J. Peřina, Ed. (Wiley, 2001), sec. 7.3.

53. S. Scheel, S. Y. Buhmann, Macroscopic quantum electrodynamics—Concepts and applications. *Acta Phys. Slovaca* **58**, 675 (2008). doi:10.2478/v10155-010-0092-x

54. L. Novotny, B. Hecht, *Principles of Nano-Optics* (Cambridge Univ. Press, 2012).

55. J. Shapiro, G. Breit, Metastability of 2s states of hydrogenic atoms. *Phys. Rev.* **113**, 179–181 (1959). doi:10.1103/PhysRev.113.179